Sensors and Materials, Vol. 32, No. 10 (2020) 3383–3397
MYU Tokyo

S & M 2346

Effects of Heat Generated during Grind Hardening on Hardness and Microstructure of Alloy Metal: Optimal Process to Improve Efficiency

Shunxing Gao,[1] Judong Liu,[1,2*] Songwei Huang,[1] and Rongchuan Lin[1**]

[1]School of Mechanical and Energy Engineering, Jimei University,
No. 9 Shigu Road, Jimei District, Xiamen, Fujian 361021, China
[2]Key Technology Engineering Research Center of University Marine Platform Guarantee System
of Fujian Province, Xiamen, Fujian 361021, China

(Received April 22, 2020; accepted August 25, 2020)

Keywords: grind hardening, hardness, microstructure, regrinding value, softening zone, steel

Grind hardening is an alternative process to the conventional quenching process. The heat generated during grinding transforms the surface layer of workpieces into the martensitic structure. In this study, we simulated the temperature distribution during grind hardening to investigate the effects of heat on the changes in hardness and microstructure with different regrinding values using AISI 5140 alloy metal. We also compared the experimental results of single- and double-pass grind hardening processes. The results showed that the regrinding value affected the lateral distribution of hardness on the surface of the metal during grind hardening. The process created a softening width between the first and second ground layers, where a decreased softening width indicated the improved efficiency of grind hardening. It was found that double-pass grind hardening yielded the desired grinding results that reduced the softening width. The results of this study obtained using the AISI 5140 alloy metal also suggest that double-pass grind hardening can be used in high-efficiency quenching for various alloy metals.

1. Introduction

Grind hardening is a manufacturing process in which the heat generated by grinding is used for rapid heating to quench the surface of steel with the self-cooling of the steel.[(1–3)] Simultaneous grinding and quenching is regarded as a green manufacturing technology and increasingly adopted nowadays.

Previous studies on grind hardening have mainly investigated the properties of grind-hardened surfaces since Brinksmeier and Brockhoff first proposed the idea of the surface hardening of steel during grinding and verified the feasibility and effectiveness of the process.[(2)] After that, Brockhoff and Brinksmeier investigated factors affecting the efficiency of grind

*Corresponding author: e-mail: liujd2006@163.com
**Corresponding author: e-mail: rongchuanchina@sina.com

https://doi.org/10.18494/SAM.2020.2929

hardening for the AISI 4140 alloy metal, including the depth of cut, the type of grinding wheel, alloying elements, the carbon content, and the pretreatment of the grind-hardened layer.[3] Zarudi and Zhang studied the changes in the layer structure, wear resistance, and bending fatigue of grind-hardened steel to propose a model for the vertical change in the hardened layer structure of the AISI 4140 alloy metal.[4,5] Nguyen and coworkers studied the microstructure, hardness, and residual stress development of a grind-hardened layer using cooling media, such as dry air and liquid nitrogen,[6] and suggested a model for determining the grind-hardened depth under different cooling conditions.[7] Liu and coworkers found appropriate parameters for the microstructure, the mechanical uniformity, the hardness, and the depth of the hardened layer for single-pass or double-pass grinding.[8–10] Liu *et al.* found that the martensitic structures and microhardness of the hardened layer of 65Mn steel do not change notably.[8] Liu *et al.* considered that there are some arc-shaped medium/high-temperature tempered zones, and some annular unhardened zones in the external circumference surface layer, which are the result of a temperature gradient, induced grinding heat when circumferential feed and axial grinding heat conduction occur in a plunge cylindrical grinding process.[9] Liu *et al.* concluded that the quality of grinding and hardening could be improved with a large depth of cut and a low table speed and combined with the up-down or down-up-down grinding method, which could effectively control the depth and uniformity of the hardened workpieces for 65Mn steel.[10] Several researchers proposed models to determine the temperature distribution in hardened layers of 40Cr and 45 steel with segmented triangular heat sources.[11–14] Huang and coworkers found a way to minimize the use of lubricants for grind hardening with variable grinding forces for the AISI 5140 alloy metal.[15–17] These results provide the information required to improve grind hardening to achieve a higher efficiency and a more environmentally friendly manufacturing process.

However, these investigations mainly focused on single-pass grind hardening, which is limited to small workpieces and a single-pass process. Thus, we aimed to study the changes, effects, and results of double-pass grind hardening on the surface of an alloy metal. We also attempted to find an appropriate method of high-temperature measurement to determine the surface temperature distribution during the process. The results of this study are expected to clarify the effects of regrinding on the changes in hardness and microstructure in the surface layer of an alloy metal and the influence of temperature on these effects. The information necessary to develop a more advanced grind hardening process is also provided.

Li *et al.* described a fiber-optic temperature sensor based on the interference of selective high-order modes, which can be used for high-temperature measurements.[18] Byrne and Lim reviewed an ingestible telemetric body-core temperature sensor and found that attention should be paid to ensure adequate control over sensor calibration and data correction, the timing of ingestion, and electromagnetic interference.[19] Zhu and Zeng conducted a comprehensive review of the room-temperature gas sensing properties of ZnO-based gas sensors and indicated that a large number of photoinduced electrons under light illumination improve electrical behaviors, resulting in the room-temperature gas sensing of ZnO-based gas sensors.[20] Navale *et al.* used zinc oxide hierarchical nanostructures as potential NO_2 sensors. They showed that for the lowest NO_2 concentration in their study (1 ppm), the zinc oxide sensor showed good response in terms of speed and recovery time.[21]

However, none of the above works discussed the surface temperature detection of a grind-hardening workpiece using temperature sensors. Here, we aim to detect the surface temperature distribution of a workpiece using temperature-sensing technology to avoid diverse thermal damage, including local grinding, burning, microcracking, and thermal softening on the surface of the workpiece. The sensor should be suitable for high-temperature measurements.

The sensor used to measure the surface temperature of the workpiece can obtain the temperature distribution of the surface zone of workpieces. The measuring principle is that of thin-film thermocouples. Thin-film thermocouples are directly prepared on the surface of the structure using thin-film deposition techniques and include an insulating layer and a device layer to achieve in situ measurements of the surface transient temperature.[22] Therefore, thin-film thermocouples are perfect for this test sensor.

2. Methods

2.1 Grinding method

We used single-pass and double-pass grind hardening processes to compare the difference in the lateral distribution of the generated heat and the microstructure of the ground regions. Single-pass grinding (the first pass of grinding in this study) involves the reciprocating movement of a grinder along the length of a steel workpiece, while double-pass grinding (the second pass of grinding in this study) involves moving a certain distance along the width of the workpiece after reciprocating grinding [Figs. 1(a) and 1(b)]. For the two different grind hardening processes, we defined the regrinding width C_r as in Fig. 1(c).

The grinding processes were conducted with an M7130 surface grinder and a WA60L6V vitrified-white-corundum grinding wheel (manufactured by Tengzhou Uni-tech Co., Ltd. and Keihin Kogyo Co., Ltd., respectively). The wheel was 340 mm in diameter and 40 mm in width. We performed double-pass grinding with a grinding wheel speed of 1440 revolutions per minute (rpm), a wheel speed (v_s) of 25.6 m/s, a depth of cut (a_p) of 300 μm, and a table speed (v_w) of 0.6 m/min. The effective grinding volume was 100 × 10 × 15 mm^3 with a single-pass grinding width of 5 mm and a second-pass grinding width of 5, 6, 7, or 8 mm. The regrinding value

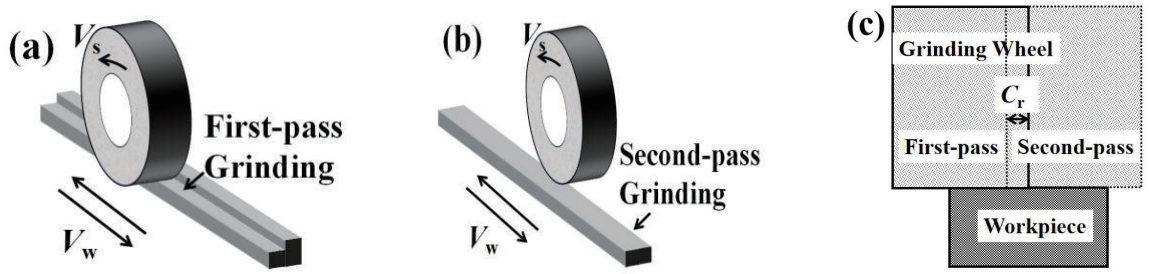

Fig. 1. Schematics of double-pass grinding. (a) First-pass grinding. (b) Second-pass grinding. (c) Transverse section.

(C_r) was 0, 1, 2, or 3 mm. All the processes in this study were conducted at room temperature without a coolant. The process and conditions of grind hardening are described in detail in Fig. 2 and Table 1. Prior to each test, the wheel was dressed using a point diamond dresser. We repeated each experiment three times.

Figure 2 shows the components of the grinding wheel, jig, workpiece, temperature sensor, and worktable. A temperature sensor (Fig. 2) was used to detect the surface temperature of the workpiece during the test to ascertain whether the surface of the workpiece exhibited the burning phenomenon.

2.2 Temperature measurement

Figure 3 shows the system used to measure the surface temperature. The temperature was measured using a sensor that converted the measured data into output signals. The signals were collected and sent to a system to monitor the temperature and prevent the surface metal from burning.

The novelty of this paper lies in the theory and the experiment using the temperature-sensing measurement technology. Firstly, the structure and hardness generation mechanism in the softening zone are revealed using the temperature-sensing measurement technology. Secondly,

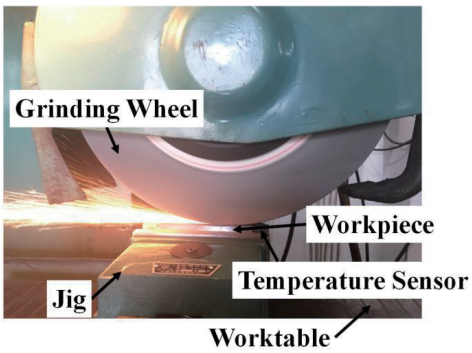

Fig. 2. (Color online) Experiment on grind hardening.

Table 1
Grinding conditions of the experiments.

Wheel material / grade	White corundum / WA60L6V
Wheel diameter (mm)	340
Wheel speed (rpm)/(m/s)	1440/25.6
Workpiece material	AISI 5140 steel
Workpiece size (mm^3)	100 × 10 × 15
Dressing	Single-point diamond
	Total dressing depth = 3 × 25 μm
Grinding mode	Up-grinding + Down-grinding
Depth of cut (μm)	300
Table speed (m/min)	0.6
First-grinding width (mm)	5
Second-grinding width (mm)	5, 6, 7, 8
Regrinding value (mm)	0, 1, 2, 3

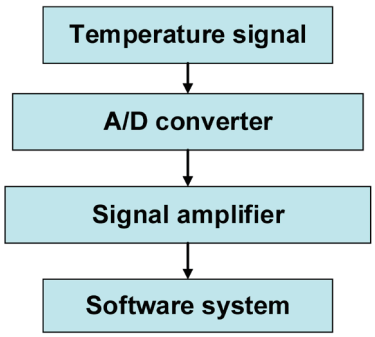

Fig. 3. (Color online) Temperature measurement system.

the desired grinding results are obtained over a large area in a surface grind-hardening experiment by double-pass grind hardening.

2.3 Tested alloy metal

AISI 5140 alloy metal with a Vickers pyramid hardness of 220 ± 15HV was selected for the experiment. The major components of the AISI 5140 alloy metal are presented in the macrograph and micrograph images shown in Figs. 4(a) and 4(b), respectively. As can be seen from Fig. 4(b), the white part of the matrix is lath pearlite and the other part is ferrite. The chemical composition and nominal phase transformation temperature A_{c1} (747 °C) of the AISI 5140 alloy metal are shown in Table 2.[12]

2.4 Hardness, microstructure, and composition

The ground workpiece was sliced with a wire electrical discharge machine (WEDM) with sufficient coolant to avoid thermal disturbances. The locations of the sliced pieces are illustrated in Fig. 5. The depth of the grind-hardened layer was measured. The pieces were mounted in an XQ-2B hot press and polished with a PA-2 polisher. The fine-polished workpieces were etched with 4 mL of nitric acid in 96 mL of ethanol to observe the microstructures of the ground and inner (unground) layers of the AISI 5140 alloy metal. The hardness of the ground workpieces

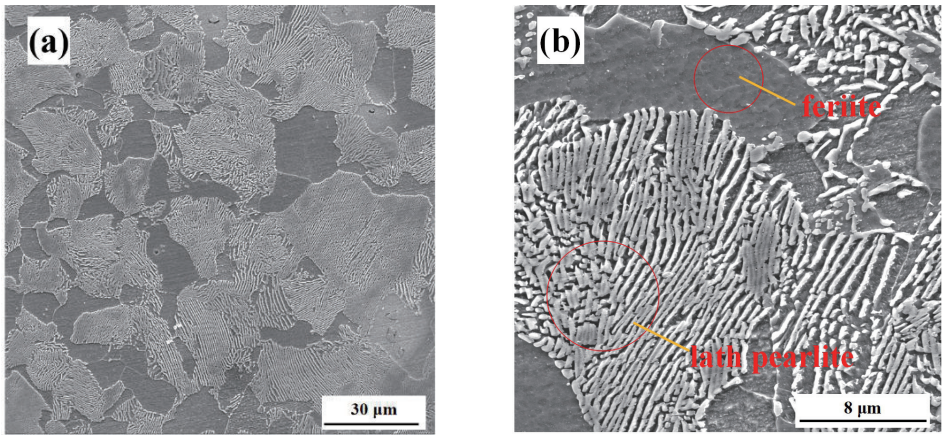

Fig. 4. Major components of AISI 5140 alloy metal. (a) Macrograph image. (b) Micrograph image.

Table 2
Chemical composition and physical properties of AISI 5140 alloy metal.

Chemical constituent (%)		Physical properties	
C	0.40	A_{c1} (°C)	747
Mn	0.65	A_{c3} (°C)	784
Cr	0.95	Density ρ (kg/m^3)	7.87×10^3
Ni	0.06	Fusion point	1400 °C
Si	0.25		

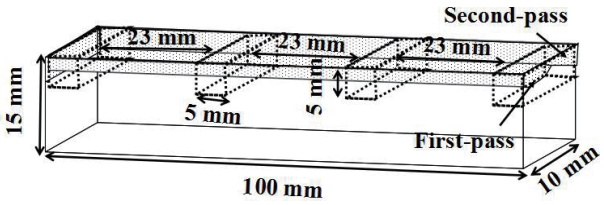

Fig. 5. Locations of sliced pieces.

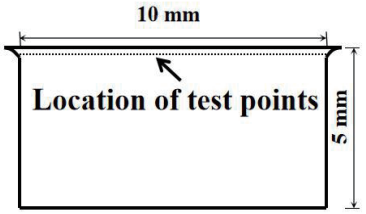

Fig. 6. Hardness detection position along the width direction.

was measured using an HX-1000TMC hardness tester at a load of 1000 gf at a depth of 0.1 mm from the surface (Fig. 6). The thickness and morphology of the layer were examined using a metallurgical microscope (VK-X100K), and the microstructures were analyzed with a scanning electron microscope (Phenom-XL) at 15 kV.

2.5 Temperature simulation

According to the law of energy conservation, the equation of three-dimensional transient heat conduction is expressed as

$$\partial\theta / \partial t = \lambda / (\rho c_p) / (\partial^2\theta / \partial x^2 + \partial^2\theta / \partial y^2 + \partial^2\theta / \partial z^2 + \bar{q}_w / \lambda), \tag{1}$$

where θ, t, λ, ρ, c_p, and q_w are the transient temperature, time, thermal conductivity, density, specific heat, and average heat flux transferred into the workpiece, respectively.[23]

The contact length between the workpiece and the grind-hardening wheel is defined as

$$l_c = \sqrt{d_e a_p}, \tag{2}$$

where d_e and a_p are the equivalent diameter and the depth of cut, respectively.[24]

The heat flux q is calculated as

$$q = \varepsilon F_t V_s / b l_c s(x), \tag{3}$$

where F_t, V_s, b, and $s(x)$ are the tangential force, wheel speed, grind-hardening width, and grind-hardening heat flux distribution shape function, respectively.[25] In addition, ε is the heat partition of the energy entering the workpiece and is given as 0.76.[26]

Then, the following tangential force is induced:

$$F_t = b \cdot a_p (v_w / v_s) \cdot (u_{ch} + 28.1 / a_p \cdot v_w), \tag{4}$$

where u_{ch} is indicative of the specific cutting energy of 13.8 J/mm^3.[27]

With these equations, we created an algorithm for temperature simulation and calculated the temperature and its lateral distribution by finite element analysis (FEA), as shown in Fig. 7.

3. Results and Discussion

3.1 Surface morphology

The surface morphology and the results of the temperature simulation for the samples ground with the first and second passes of grind hardening are shown in Figs. 8–11. In Figs. 8(a), 9(a), 10(a), and 11(a), the surface morphologies on the left of the sliced samples are from the first pass of grind hardening, while those on the right are from the second pass. Figures 8(b), 9(b), 10(b), and 11(b) show the results of the temperature simulation of the first pass, and Figs. 8(c), 9(c), 10(c), and 11(c) show the results of the temperature simulation of the second pass. The isothermal lines in Figs. 8(c), 9(c), 10(c), and 11(c) obtained from the temperature simulation are identical to the surface morphology obtained from the experimental results [Figs. 8(a), 9(a), 10(a), and 11(a)].

There are three different zones with different shades of gray in Figs. 8(a), 9(a), 10(a), and 11(a): dark gray (hardened layer), yellow-gray (transition layer), and light gray (matrix). The depth of the hardened layer of the sliced samples increases with C_r on both the left side (the first-pass hardened layer) and the right side (the second-pass hardened layer). There is an unhardened zone between the first-pass and second-pass hardened layers for C_r of 0 mm. However, transition zones are observed between the first-pass and second-pass hardened layers for $C_r \geq 1$ mm, and the width of the transition zone increases with C_r.

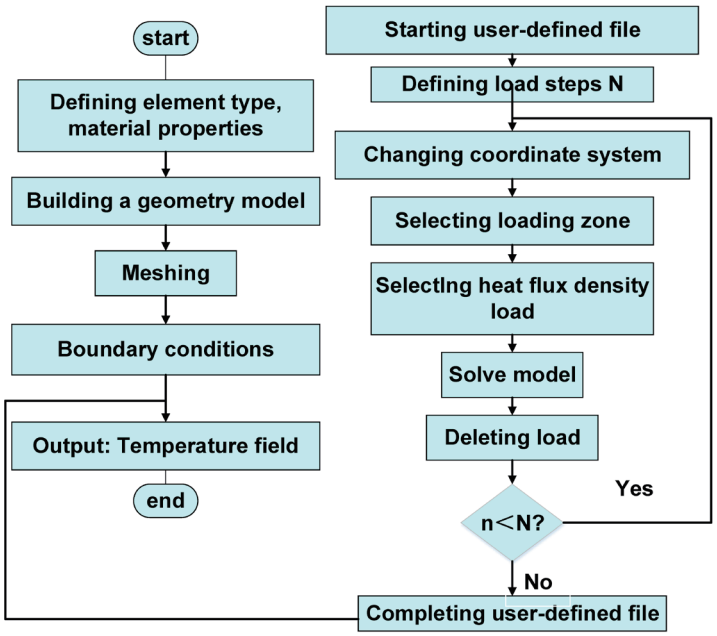

Fig. 7. (Color online) Algorithm for temperature modeling.

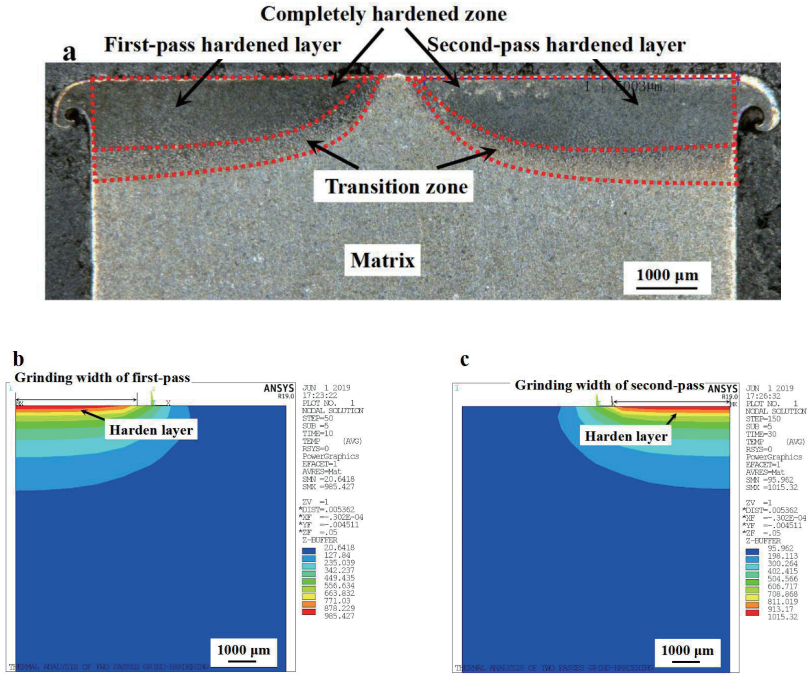

Fig. 8. (Color online) Surface topography (a_p = 0.3 mm, v_w = 0.6 m/min, and C_r = 0 mm) obtained from (a) the experiment and the ANSYS temperature simulation of the (b) first- and (c) second-pass grind hardening processes along the width direction.

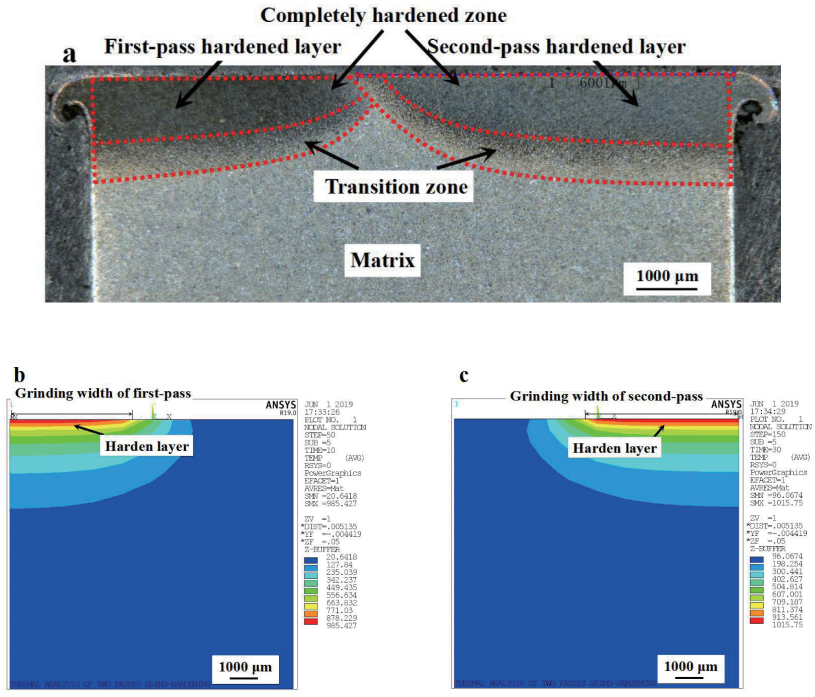

Fig. 9. (Color online) Surface topography (a_p = 0.3 mm, v_w = 0.6 m/min, and C_r = 1 mm) obtained from (a) the experiment and the ANSYS temperature field simulation of the (b) first- and (c) second-pass grind hardening processes along the width direction.

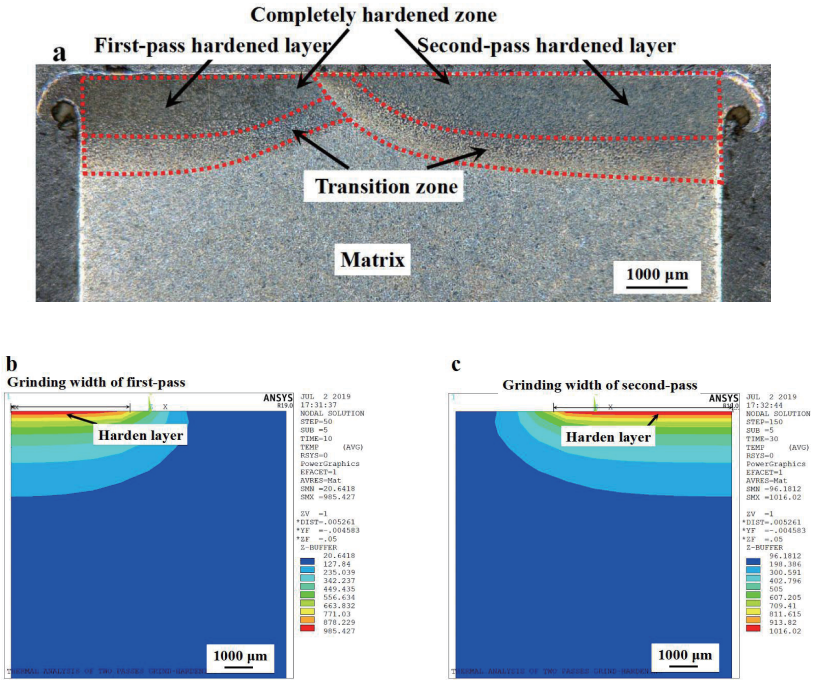

Fig. 10. (Color online) Surface topography (a_p = 0.3 mm, v_w = 0.6 m/min, and C_r = 2 mm) obtained from (a) the experiment and the ANSYS temperature field simulation of the (b) first- and (c) second-pass grind hardening processes along the width direction.

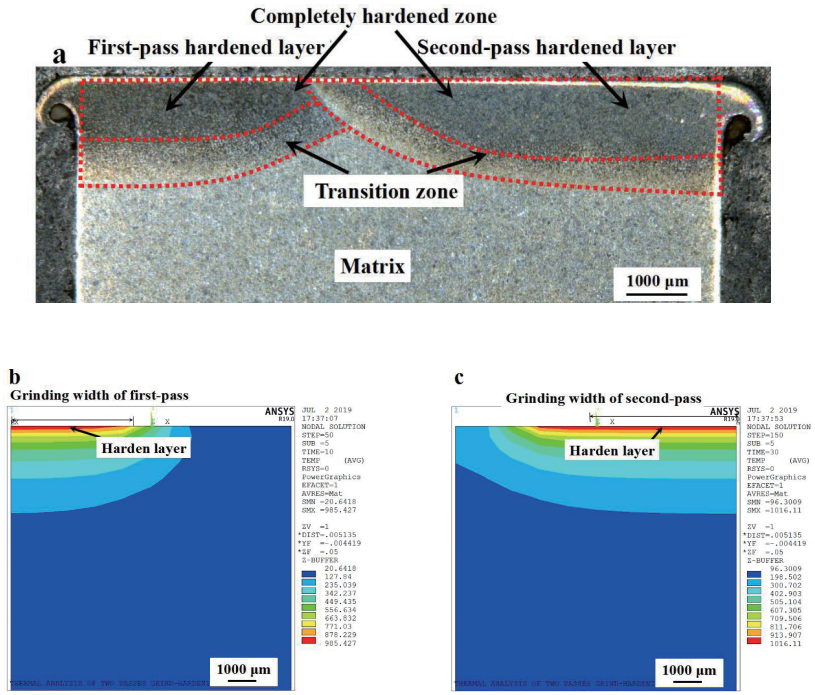

Fig. 11. (Color online) Surface topography (a_p = 0.3 mm, v_w = 0.6 m/min, and C_r = 3 mm) obtained from (a) the experiment and the ANSYS temperature field simulation results of the (b) first- and (c) second-pass grind hardening processes along the width direction.

3.2 Changes in temperature distribution and composition of surface layer

The heat in the grind-hardening region is generated vertically from the subsurface of the workpiece and laterally from the region to the ends of both sides. This creates the temperature gradients in Figs. 8–11. We can obtain information from the figures. The zone with a temperature higher than A_{c1} becomes larger, while that with a temperature lower than A_{c1} becomes smaller. This results in the vertical and lateral distributions of hardened and transition layers shown in Figs. 8(a), 9(a), 10(a), and 11(a). The completely hardened layer has a quenched martensitic structure at the austenitization temperature of A_{c3}. However, the transition layer at temperatures between A_{c3} and A_{c1} has less of the martensitic structure and more of other microstructures. The effect of the grind-hardening heat in the transition layer increases with C_r.

3.3 Temperature and hardness distributions

The distributions of hardness and temperature with distance for different C_r values are shown in Fig. 12. The distance was measured from the end of the first-pass grind-hardened layer.

In general, the lateral distribution of hardness decreases, then rapidly increases to a stable level from the first-pass to the second-pass grind-hardened layer. The lateral distribution curve of hardness with $C_r = 0$ mm in Fig. 12(a) is divided into five zones: the first hardened zone (zone I), the tempering zone (zone II), the unhardened zone (zone III) in the single-pass grind-hardened layer, the transition zone (zone IV), and the second hardened zone (zone V) in the second-

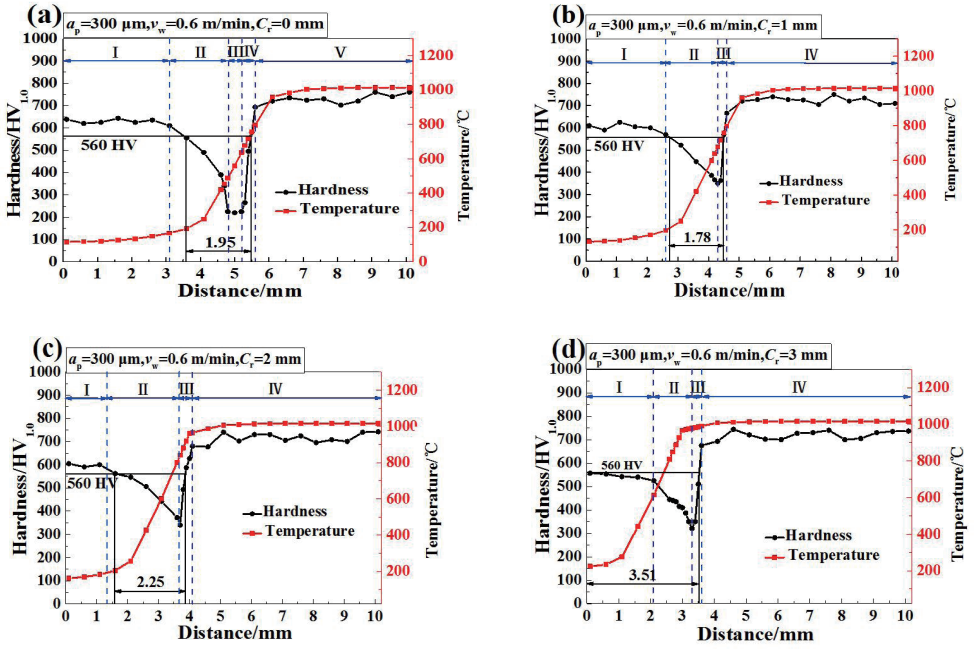

Fig. 12. (Color online) Hardness distribution curve along the component's width direction and temperature–time curve of the second-pass grind-hardened layer surface for different C_r values. (a) $C_r = 0$ mm, (b) $C_r = 1$ mm, (c) $C_r = 2$ mm, and (d) $C_r = 3$ mm.

pass grind-hardened layer. The lateral distributions with C_r = 1, 2, and 3 mm respectively illustrated in Figs. 12(b)–12(d) are divided into four zones: the first hardened zone (zone I), the tempering zone (zone II) in the first-pass grind-hardened layer, the transition zone (zone III), and the second hardened zone (zone IV) in the second-pass grind-hardened layer. The average hardness of zone I is consistently lower than that of zones IV and V, and slightly decreases with increasing C_r. The slope and width of zone II are steeper and smaller than those of zone IV, respectively.

The lateral distribution of hardness is a comprehensive consequence of the temperature distribution during the second pass of grind hardening. The temperature increases in the second pass of grind hardening owing to the heat from the first pass of grind hardening. The heat causes the dissolution of carbide, which increases the austenite's carbon content and makes the martensite supersaturated. Therefore, an increase in hardness occurs in zones IV and V. The first-pass grind-hardened layer is affected by the grind-hardening heat through lateral conduction. This leads to different degrees of heat transfer and the decrease in the hardness of the first-pass grind-hardened layer.

3.4 Softening width

The hardness penetration depth (HPD) is defined as the distance from the surface of a workpiece where the hardness is reduced to 80% of the normal value.[28–30] This means that the hardened layer has a hardness exceeding HV560. Therefore, the zone with a hardness lower than HV560 is defined as the "softening zone". The softening widths at different C_r values are shown in Fig. 13. The softening width is about 1.95 mm for C_r = 0 mm and increases with C_r. The results of the experiments confirmed that there was an unhardened zone in the workpiece for C_r = 0 mm that increased the softening width.

3.5 Microstructure of grind-hardened surface layer

According to the above results, the lateral structure for C_r = 0 mm was divided into five zones, while that for $C_r \geq 1$ mm was divided into four zones (Fig. 10). The SEM images for C_r of 0 or 1 mm revealed the following microstructure (Figs. 14 and 15): zone I (hardened zone)

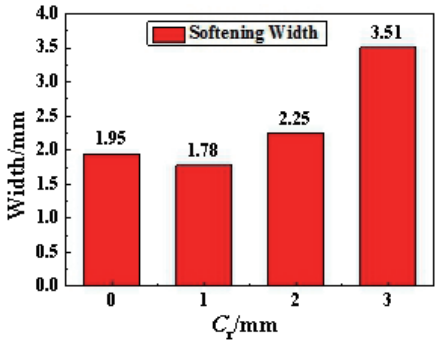

Fig. 13. (Color online) Softening widths at different C_r values.

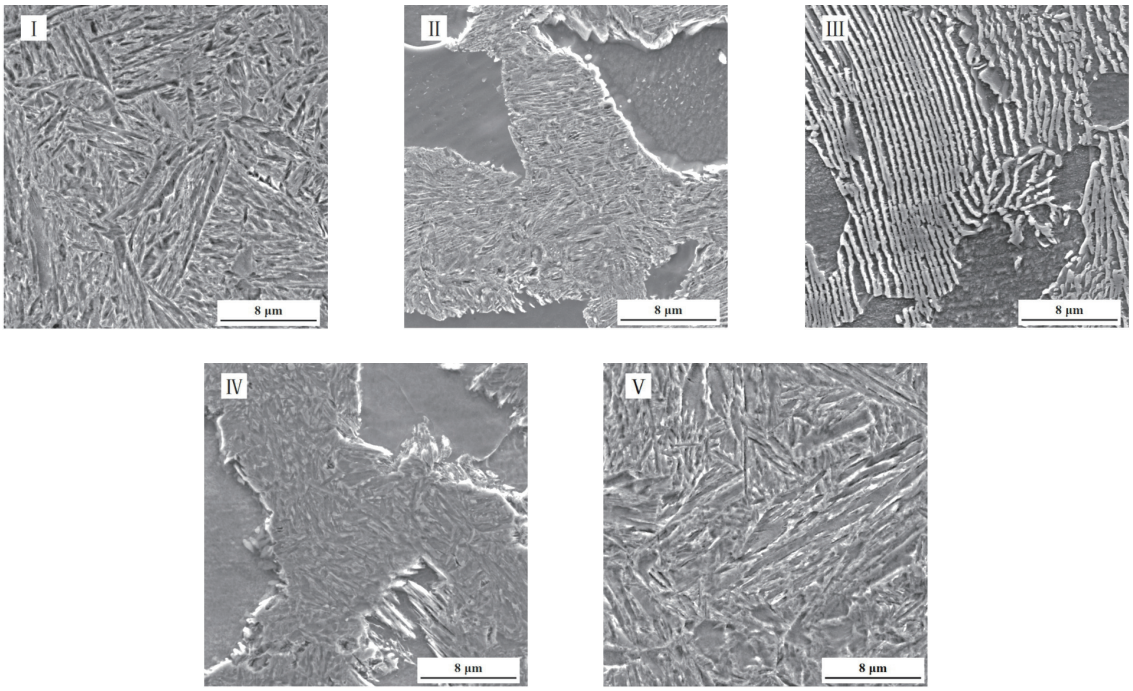

Fig. 14. SEM images with a_p = 0.3 mm, v_w = 0.6 m/min, and C_r = 0 mm. (I) First hardened zone (zone I), (II) tempering zone (zone II), (III) unhardened zone (zone III) in the first-pass grind-hardened layer, (IV) transition zone (zone IV), and (V) second hardened zone (zone V) in the second-pass grind-hardened layer.

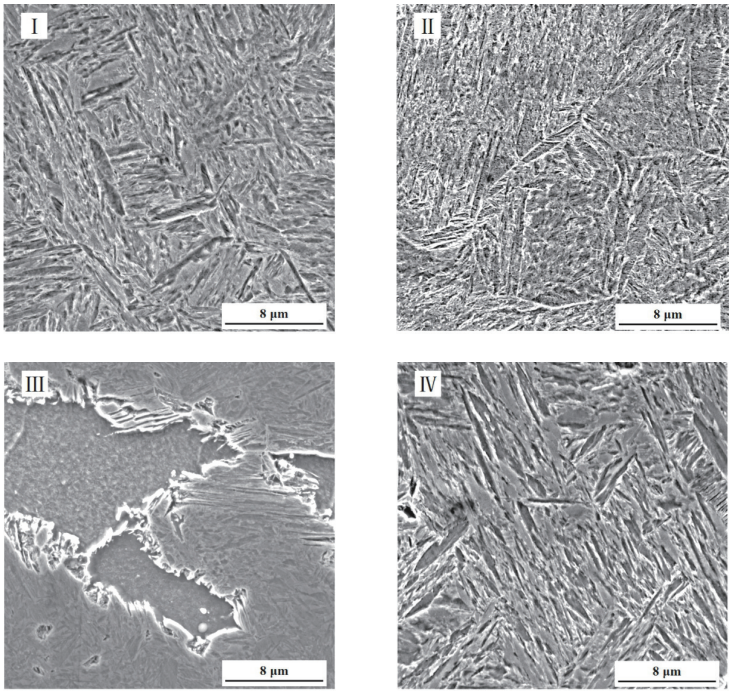

Fig. 15. SEM images with a_p = 0.3 mm, v_w = 0.6 m/min, and C_r = 1 mm. (I) First hardened zone (zone I), (II) tempering zone (zone II) in the first-pass grind-hardened layer, (III) transition zone (zone III), and (IV) second hardened zone (zone IV) in the second-pass grind-hardened layer.

Table 3
Comparison with other measurement temperature methods.

Method	Experimental measurement	Simulation prediction	Application to grind hardening
This paper	√	√	√
Ref. 18	√	×	×
Ref. 19	√	×	×
Ref. 20	√	×	×
Ref. 21	√	×	×
Ref. 22	√	×	×

was composed of martensite with a small amount of undissolved carbide, zone II (tempering zone) was composed of tempered martensite, troostite, or sorbate, zone III in the first pass of grind hardening (unhardened zone) had a matrix structure, and zone IV (transition zone) was composed of pearlite, ferrite, and a small amount of martensite. This microcomposition was in good agreement with the zones of different hardnesses.

3.6 Comparison of research methods used between this study and other studies

Table 3 shows a comparison of research methods used between this study and other studies. It can be seen that the experimental measurement and simulation prediction technology used in this study can obtain the surface temperature distribution of the workpiece during grind hardening. Only experimental measurements with no application to the grind-hardening field have been reported in the literature.[18–22] In addition, no simulation-based predictions have been reported.[18–22]

4. Conclusions

In this study, we investigated the effects of the heat generated during grind hardening on the hardness and microstructure of AISI 5140 alloy metal. We found that C_r affected the lateral distribution of hardness on the surface of the block in double-pass grind hardening. During the process, softening occurred at the transition layer between the first and second grind hardening processes owing to the lateral conduction of heat. The width of the softening zone changes with the change in C_r (C_r = 0, 1, 2, 3 mm), and the width of the softening zone is the smallest when C_r = 1 mm. The decreased width indicated the improved efficiency of grind hardening. The microstructure of the softening zone included tempered troostite, sorbite, and ferrite. We proposed a finite element analysis (FEA) model to simulate and estimate the tempering effect caused in the second grind hardening. The temperature distribution obtained by simulation was similar to that obtained in our experiment. Through this study, we found that the desired grinding results are obtained with double-pass grind hardening, which can reduce the softening width to improve the efficiency of the process. The results of this study obtained with the AISI 5140 alloy metal also suggest that double-pass grind hardening can also be used in the high-efficiency quenching of 65Mn steel, 40Cr steel, 45 steel, 42CrMo steel, GCr15 steel, and EN26 steel.

Acknowledgments

This paper was supported by the National Natural Science Foundation of China (Grant No. 51676085) and the Science and Technology Project of Fujian Province (Grant Nos. 2018J01489 and 2019J01327). It was also supported by the Natural Science Foundation of Fujian Province, China (2019J01709) and Major Science and Technology Projects in Xiamen (3502Z20191022).

Conflict of Interest

The authors declare that they have no conflicts of interest.

References

1 I. Zarudi and L. C. Zhang: J. Mater. Sci. **37** (2002) 3935. https://doi.org/10.1023/A:1019671926384
2 E. Brinksmeier and T. Brockhoff: CIRP. Ann. Manuf. Techn. **45** (1996) 283. https://doi.org/10.1016/S0007-8506(07)63064-9
3 T. Brockhoff and E. Brinksmeier: Grind-hardening: a comprehensive view. CIRP Ann. Manuf. Tech. **48** (1999) 255. https://doi.org/10.1016/S0007-8506(07)63178-3
4 I. Zarudi and L. C. Zhang: J. Mater. Sci. **37** (2002) 3935. https://doi.org/10.1023/A:1019671926384
5 I. Zarudi and L. C. Zhang: J. Mater. Sci. **37** (2002) 4333. https://doi.org/10.1023/A:1020652519141
6 T. Nguyen, I. Zarudi, and L. C. Zhang: Int. J. Mach. Tools. Manuf. **47** (2007) 97. https://doi.org/10.1016/j.ijmachtools.2006.02.010
7 T. Nguyen and L. C. Zhang: Adv. Mater. Res. **76** (2009) 3. https://doi.org/10.4028/www.scientific.net/AMR.76-78.3
8 J. D. Liu, G. C. Wang, Z. Wang, and S. T. Fan: Mater. Sci. Forum **505** (2006) 787. https://doi.org/10.4028/www.scientific.net/MSF.505-507.787
9 J. D. Liu, J. Z. Zhuang, and Z. L. Xu: Key. Eng. Mater. **621** (2014) 140. https://doi.org/10.4028/www.scientific.net/KEM.621.140
10 J. D. Liu, W. Yuan, J. K. Xiong, and S. W. Huang: Key Eng. Mater. **522** (2012) 87. https://doi.org/10.4028/www.scientific.net/KEM.522.87
11 Y. Guo, S. Xiu, M. Liu, and X. Shi: Int. J. Adv. Manuf. Technol. **89** (2017) 2001. https://doi.org/10.1007/s00170-016-9234-8
12 X. Zhang, S. Xiu, and X. Shi: Int. J. Adv. Manuf. Technol. **93** (2017) 4265. https://doi.org/10.1007/s00170-017-0819-7
13 S. Xiu, C. Sun, J. Duan, D. Lan, and Q. Li: Int. J. Adv. Manuf. Technol. **100** (2019) 209. https://doi.org/10.1007/s00170-018-2744-9
14 C. Sun, J. Wang, X. Kong, Y. Lu, and S. Xiu: Int. J. Adv. Manuf. Technol. **103** (2019) 4013. https://doi.org/10.1007/s00170-019-03741-y
15 X. Huang, Y. Ren, B. Zheng, Z. Deng, and Z. Zhou: J. Mech. Sci. Technol. **30** (2016) 3819. https://doi.org/10.1007/s12206-016-0745-x
16 X. Huang, Y. Ren, W. Jiang, Z. He, and Z. Deng: Int. J. Adv. Manuf. Technol. **89** (2017) 1069. https://doi.org/10.1007/s00170-016-9142-y
17 X. Huang, Y. Ren, W. Wu, and T. Li: Int. J. Adv. Manuf. Technol. **103** (2019) 1045. https://doi.org/10.1007/s00170-019-03329-6
18 E. Li, X. Wang, and C. Zhang: Appl. Phys. Lett. **89** (2006) 91. https://doi.org/10.1063/1.2344835
19 C. Byrne and C. L. Lim: Brit. J. Sport. Med. **41** (2007) 126. https://doi.org/10.1136/bjsm.2006.026344
20 L. Zhu and W. Zeng: Sens. Actuators, A **267** (2017) 242. https://doi.org/10.1016/j.sna.2017.10.021
21 Y. H. Navale, S. T. Navale, N. S. Ramgir, F. J. Stadler, S. K. Gupta, D. K. Aswal, and V. B. Patil: Sens. Actuators, B **251** (2017) 551. https://doi.org/10.1016/j.snb.2017.05.085
22 J. J. Deng, W. H. Wang, L. A. Hui, J. T. Zhang, and X. H. Jin: Sensors **19** (2019) 5. https://doi.org/10.3390/s19051155
23 S. Y. Liu, G. Yang, J. Q. Zheng, and X. H. Liu: Int. J. Adv. Manuf. Technol. **76** (2015) 487. https://doi.org/10.1007/s00170-014-6319-0

24 W. B. Rowe and M. N. Morgan: CIRP Ann. Manuf. Tech. **42** (1993) 409. https://doi.org/10.1016/S0007-8506(07)62473-1
25 L. Zhang, P. Q. Ge, J. H. Zhang, Z. J. Zhu, and Z. Y. Luan: Int. J. Abras. Technol. **1** (2007) 2. https://doi.org/10.1504/IJAT.2007.015383
26 X. Zhang, S. Xiu, and X. Shi: Int. J. Adv. Manuf. Technol. **93** (2017) 4265. https://doi.org/10.1007/s00170-017-0819-7
27 K. Salonitis, P. Stavropoulos, and A. Kolios: Int. J. Adv. Manuf. Technol. **70** (2014) 523. https://doi.org/10.1007/s00170-013-5260-y
28 G. Chryssolouris, K. Tsirbas, and K. Salonitis: J. Manufact. Proc. **7** (2005) 1. https://doi.org/10.1016/S1526-6125(05)70076-1
29 K. Salonitis and G. Chryssolouris: Int. J. Adv. Manuf. Technol. **33** (2007) 285. https://doi.org/10.1007/s00170-006-0467-9
30 K. Salonitis: Procedia CIRP **13** (2014) 264. https://doi.org/10.1016/j.procir.2014.04.045

About the Authors

Shunxing Gao received his B.S. degree from Jimei University, China, in 2017 and his M.S. degree from the School of Mechanical and Energy Engineering, Jimei University, China, in 2020. His research interests are in multiscale precision manufacturing and sensors. (shunxinggaoxm1994@163.com)

Judong Liu received his B.S. degree from Xi'an Jiaotong University, China, in 1985 and his Ph.D. degree from the School of Mechanical Engineering, Jiangsu University, China, in 2005. Since 2005, he has been a professor at Jimei University. His research interests are in multiscale precision manufacturing and sensors. (liujd2006@163.com)

Songwei Huang received his B.S. degree from Hubei University of Technology, China, in 2010. Since 2015, he has been a deputy director at Jimei University Engineering Training Center. His research interests are in grinding technology and sensors. (huangsw2015@126.com)

Rongchuan Lin obtained a master's degree in mechanical engineering from Xiamen University in 2007. In 2014, he became a professor of mechanical engineering in Jimei University, specializing in precision machining. (rongchuanchina@sina.com)